CORA Cork Open Research Archive
Cartlann Taighde Oscailte Chorcaí

Title	Investigation of transverse exchange-springs in electrodeposited nano-heterostructured films through first-order reversal curve analysis
Authors	Samanta, Arindam;Roy, Saibal
Publication date	2024-09-19
Original Citation	Samanta, A., Roy, S. (2024) 'Investigation of transverse exchange-springs in electrodeposited nano-heterostructured films through first-order reversal curve analysis', APL Materials, 12(9), 091118 (13pp). https://doi.org/10.1063/5.0223485
Type of publication	Article (peer-reviewed)
Link to publisher's version	10.1063/5.0223485
Rights	© 2024, the Authors. All article content, except where otherwise noted, is licensed under a Creative Commons Attribution (CC BY) license (https://creativecommons.org/licenses/by/4.0/). - https://creativecommons.org/licenses/by/4.0/
Download date	2026-10-30 08:23:46
Item downloaded from	https://hdl.handle.net/10468/16713



UCC
University College Cork, Ireland
Coláiste na hOllscoile Corcaigh

APL Materials

RESEARCH ARTICLE | SEPTEMBER 19 2024

Investigation of transverse exchange-springs in electrodeposited nano-heterostructured films through first-order reversal curve analysis

Special Collection: Emerging Leaders in Materials Science

Arindam Samanta ; Saibal Roy

Check for updates

APL Mater. 12, 091118 (2024)
https://doi.org/10.1063/5.0223485

View Online
Export Citation

Articles You May Be Interested In

Fractal structures in two-metal electrodeposition systems I: Pb and Zn

Chaos (December 2011)

Fabrication and magnetic properties of patterned NiFeMo films electrodeposited in self-assembled nanosphere templates

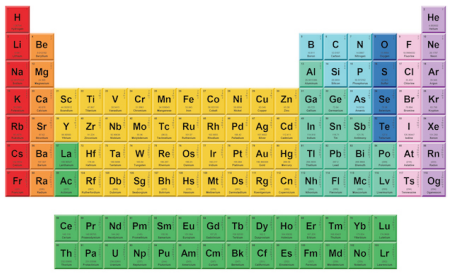
J. Appl. Phys. (March 2011)

Thick-film permanent magnets by membrane electrodeposition

J. Appl. Phys. (June 2005)

05 December 2024 14:20:21

AMERICAN ELEMENTS
THE MATERIALS SCIENCE MANUFACTURER®
Now Invent.™
27 ANNIVERSARY



American Elements
Opens a World of Possibilities
...Now Invent!
www.americanelements.com

AIP Publishing

Investigation of transverse exchange-springs in electrodeposited nano-heterostructured films through first-order reversal curve analysis

Cite as: APL Mater. 12, 091118 (2024); doi: 10.1063/5.0223485
Submitted: 14 June 2024 • Accepted: 28 August 2024 •
Published Online: 19 September 2024

View Online Export Citation CrossMark

Arindam Samanta[1,2] and Saibal Roy[1,2,a)]

AFFILIATIONS

[1] Micropower Devices and Nanomagnetics Group, Tyndall National Institute, Cork T12R5CP, Ireland
[2] School of Physics, National University of Ireland – University College Cork, Cork T12YN60, Ireland

Note: This paper is part of the Special Topic Titled Emerging Leaders in Materials Science.
[a)] **Author to whom correspondence should be addressed:** saibal.roy@tyndall.ie

ABSTRACT

The prerequisite of efficient exchange-spring nano-heterostructures, i.e., tuning both hard and soft phases at a nanometer level, has posed significant preparation challenges to ensure effective exchange-coupling. Here, we present a novel approach to fabricate transverse exchange-spring nano-heterostructures using single starting material through an "*in situ*" electrodeposition technique at room temperature. Utilizing modified acidic bath chemistry and controlled hydrogen evolution, we successfully prepared stress-free, shiny, fine-grained amorphous, and nanocrystalline Co-rich cobalt phosphorus films. These nano-heterostructured films exhibit a unique non-collinear anisotropy-driven transverse exchange-spring behavior, investigated systematically under ambient conditions. The comprehensive functional analyses reveal that intricate interplay between in-plane (IP) anisotropy of amorphous phase and out-of-plane (OOP) anisotropy generating from a nanocrystalline structure compete with each other, while producing characteristic stripe domain structures to novel corrugated stripe domain shapes. The angle-dependent first-order reversal curve distributions demonstrate new insights into the magnetic reversal mechanisms, further confirming the non-exchange-spring and exchange-spring nature of the films depending on the prevalent interfacial exchange coupling. Formation of anisotropy-driven metastable-state due to competition between IP and OOP anisotropy at a particular OOP orientation has led the normal exchange-spring structures to a transverse exchange-spring structure. Micromagnetic simulations, in excellent agreement with experimental data, further elucidate the formation of characteristic stripe domain patterns and the influence of anisotropy on the magnetic properties. The innovative methodology and detailed functional analysis presented here offer significant understanding to the field of exchange-spring magnetic materials, including anisotropy-driven metastable states, demonstrating the potential for scalable and cost-effective fabrication of advanced nano-heterostructures with tailored magnetic properties.

© 2024 Author(s). All article content, except where otherwise noted, is licensed under a Creative Commons Attribution (CC BY) license (https://creativecommons.org/licenses/by/4.0/). https://doi.org/10.1063/5.0223485

05 December 2024 14:20:21

I. INTRODUCTION

In contrast to traditional single ferromagnetic (FM) thin films, multilayered nano-heterostructures (NHSs) with sandwich-like configurations exhibit enhanced properties, such as higher coercivity (H_C) and greater saturation magnetization (M_S), resulting in an increased energy product (BH_{max}). These NHSs, termed exchange-spring (ES) systems,[1–3] are highly relevant for advanced applications in data storage, spintronics, and beyond. A crucial aspect of the formation of ES NHSs is the relative thickness of the soft phase (L_S) compared to the domain wall width (δ_H) of the hard phase. In particular, $L_S > 2\delta_H$ fosters ES behavior, while $L_S \leq 2\delta_H$ results in a single unit behavior, marked by a flat rectangular hysteresis loop indicative of exchange-coupled (EC) systems.[4] Significant research over the past three decades has been dedicated to exploring ES systems.[5–18]

Given that soft and hard magnets interact through magnetic exchange interactions at the nanometer scale, the observation

© Author(s) 2024

and analysis of domain structures are crucial for understanding their behavior. Interfaces in the ES structures significantly impact exchange coupling and magnetic anisotropy. Analyzing domain wall behavior at these interfaces reveals the nature of exchange interactions that define functionality of the ES systems. The competition between in-plane (IP) anisotropy and out-of-plane (OOP) anisotropy within the material often results in stripe domain structures.[19,20] Despite their importance, magnetic domain analyses in ES NHSs are underexplored, and it is expected that IP ES systems would lack periodic stripe domain patterns due to the absence of OOP anisotropy. A recent study attributes the formation of stripe domains to the dynamics of 90° and 180° domain wall processes, influenced by the competition between in-plane and out-of-plane anisotropy through the formation of helical anisotropy.[21] The first-order reversal curve (FORC) analysis further reveals that stripe domain formation is related to the double-sigmoid hysteresis loop observed in the material, indicating the presence of two magnetic phases with distinct coercivities, which further highlights the complex interplay of domain dynamics that leads to stripe domain formation.[21]

On the other hand, some OOP ES structures, featuring ferromagnetic and antiferromagnetic interactions, exhibit spin flop transitions.[22] These structures show maze-like domain patterns in strongly OOP systems, such as [Co/Pd]-NiFe[23] and $L1_1$ CoPt-NiFe.[24] The domain behavior of OOP [Co/Pt]/NiFe ES systems, however, remains unexplored.[25] When continuous thin films are nano-patterned to nano-meter or sub-micron dimensions, the resulting nano-modulation can dominate the film's uniaxial anisotropy, creating a competition between IP and OOP magnetic dipoles, thereby preventing vortex formation[26] although without forming the stripe domains. Notably, while the IP ES structures are well-studied, transverse ESs with OOP anisotropy are comparatively less explored.[13,22,25,27]

In this manuscript, first, we explore the preparation of stress-free, shiny, fine-grained dispersed "*in situ*" magnetic nano-heterostructures (NHSs) of a single CoP film, still a less explored avenue to the research community. This is achieved through modified stable acidic bath chemistry with controlled hydrogen evolution, a method not previously employed in the context of ES systems. This innovative approach offers a low-cost and high-yield alternative to traditional *ex situ* fabrication techniques, such as magnetron sputtering,[25] annealing,[28] ion-irradiation,[8] and molecular beam epitaxy.[22] The electroplating technique used here allows for the creation of complex nano-topologies, which are crucial for the development of advanced magnetic materials.[18,29–31] A significant contribution of this study is the demonstration of the transition from a non-ES state to a transverse-ES state within a single thin film driven by the non-collinearity of spin textures at room temperature, which reveals new insights into the magnetic behavior of ES systems, particularly those influenced by out-of-plane (OOP) anisotropy. In addition, we perform first-order reversal curve (FORC) measurements and analysis to confirm that the developed ES system is driven by anisotropy induced by OOP anisotropy, leading to the formation of novel stripe domain patterns. These findings are further corroborated by micromagnetic simulations using MuMax^3,[32] providing a robust theoretical framework to support our experimental results.

TABLE I. Plating bath composition and conditions.

Component	Amount (g/100 ml)	
	Old Bath[33]	New bath
Phosphorus acid (H_3PO_3)	3.00	3.30
Phosphoric acid (H_3PO_4)	5.00	5.90
Cobalt chloride hexahydrate ($CoCl_2 \cdot 6H_2O$)	18.00	18.87
Cobalt carbonate ($CoCO_3$)	1.50	1.55
Glycine	···	1.15
Saccharine	···	1.51
NTA	···	1.52
Temperature	345 K	293 K
pH	0.75	0.72–86

II. EXPERIMENTAL METHODS

We have developed smooth, shiny, amorphous-nanocrystalline cobalt phosphorus (*CoP*) films by using the DC electrodeposition technique. The following chemicals and reagents, phosphorus acid, phosphoric acid, cobalt chloride hexahydrate, cobalt carbonate,[18,33] as presented in Table I, form the required electrolytic plating bath. The thin films developed from the bath are quite stressed and rough, possibly due the instability of the bath and the high surface tension between the working electrode (WE) and the electrolyte. Therefore, we have added a surface tension reducing agent, glycine, in order to stabilize the bath, and stress-relieving additives, naphthalene trisulfonic acid (NTA) and saccharine[18] reduce the surface tension between the WE and electrolyte to the solution. Consequently, stress-free, smooth, glossy thin films are developed. The modified and stable bath compositions are presented in Table I.

We carry out electrodeposition by varying the current density from 5 to 40 mA/cm^2 and keeping the deposition time fixed for 120 min. We have performed the micro-structural and elemental characterization of the electrodeposited films using ZEISS scanning electron microscope (SEM)–energy dispersive x-ray spectroscopy (EDX) analysis (Oxford Instruments). We have characterized the XRD (x-ray diffraction) patterns in Panalytical X'Pert Pro MRD with Cu Kα radiation (40 kV, 50 mA) at a wavelength of 1.54 nm. The HR-TEM (high-resolution Transmission electron microscopy) characterization was done using JEOL TEM 2100. The HR-TEM lamella cross sections were prepared using a dual-beam focused ion beam (FIB), FEI Helios NanoLab 600i. A 50 nm C layer and 300 nm Pt layer were deposited within the dual-beam FIB by electron beam induced deposition and a 2 μm thick Pt layer with ion beam induced deposition. These three layers are for protection before the FIB milling process. The lamella was prepared and thinned down for the HR-TEM analysis. The thinning at 30 kV was finished with a final polishing at 5 kV (47 pA) to reduce the ion-beam induced damage to a less than 2 nm thin layer on both sides. Micro-structural analysis was performed using an HR-TEM (Jeol 2100 transmission electron microscope; 200 kV using a double-tilt sample holder. 3D surface profiles (roughness) and magnetic force microscopy imag-

05 December 2024 14:20:21

© Author(s) 2024

ing (MFM) of the films were studied using a Bruker Dimension Icon AFM (atomic force microscopy).

The magnetic measurements were carried out using a hysteresis loop tracer (MESA 200, ShB Instruments, USA) for ±1000 Oe for the hysteresis loops and a Superconducting QUantum Interference Device (SQUID) magnetometer [Quantum Design Magnetic Property Measurement System (MPMS), Model: MPMS3] for the first-order reversal curve (FORC) measurements. A total of 200 FORCs were measured for each sample using the SQUID MPMS3 system. The required FORC measurement sequence and the subsequent data-processing were done by a code (Python) developed in-house and the FORC diagrams in the (H_C, H_U) plane were constructed utilizing FORCinel software.[34] Each of the FORC measurements involved saturating the sample and then measuring the moment from a reversal field H_R back to positive saturation field ($+H_S$), yielding a family of FORCs for different values of H_R with an increasing field of H_F spaced equally. It is important to note that H_F represents the applied magnetic field during each minor loop within the FORC measurement, whereas the field spacing refers to the incremental steps between successive applied fields in the FORC analysis. The following mixed second-order derivative expression obtained the FORC distribution, $\rho(H_R, H_F)$:

$$\rho\ (H_R, H_F) = -\frac{1}{2M_S}\left(\frac{\partial^2 M(H_R, H_F)}{\partial H_R \partial H_F}\right),$$

where M_S is the saturation magnetization. This eliminates the pure reversible components of magnetization, and any non-zero ρ corresponds to irreversible switching processes in the system.[35–37] The FORC distribution [$\rho\ (H_C, H_U)$] is presented in the (H_C, H_U) plane, where $H_C = \frac{1}{2}(H_R - H_F)$ and $H_U = \frac{1}{2}(H_R + H_F)$ represent the local coercivity and the interaction or bias field, respectively. It could be noted that the FORCinel fits the magnetization data [M(H_R, H_F)] with a second-order polynomial function following the modified algorithm, the locally weighted regression smoothing technique, often referred to as "LOESS,"[34] where the degree of smoothing is specified by a factor α, defined as

$$\alpha = \frac{(2SF+1)^2}{N_{obs}},$$

where SF is the effective smoothing factor and N_{obs} is the number of magnetic measurements in the M(H_R, H_F) matrix. In order to obtain the effective SF, we utilized the in-built "explore optimum smoothing factor" function and considered the lowest obtained value from the fit to construct the FORC diagrams.[34] The aforementioned algorithm yields that the optimal smoothing factor (SF) for constructing FORC diagrams is 4, unless otherwise specified. For instance, the SF for 30°, 60°, and 90° FORC distributions are 4.35, 6.15, and 5.5, respectively.

III. RESULTS AND DISCUSSION

A. "*In situ*" NHS formation by hydrogen evolution

The transfer of electrons in an electrochemical process induces the chemical change, such as the oxidation or reduction of a metal complex. Here, the anode represented by *Co* undergoes an oxidation process to form Co^{3+} ions via heterogeneous electron transfer. The schematic of this oxidation process is shown in Fig. 1(a). Conversely, the reduction process of reduced phosphorus (P) follows a reverse phenomenon, as shown in Fig. 1(a) and is described below.

We perform the widely used electrochemical technique of three-electrode cyclic voltammetry (CV) analysis, schematically shown in Fig. 1(b), in order to investigate the possible reaction processes. Here, a piece of 2 × 2 cm^2 Si wafer, featuring top-conducting sputtered Ti/Au (20/200 nm) seed layers, serves as the working electrode (WE) and a Co-piece functions as the counter electrode (CE). The voltage of the working electrode is referenced to Ag/AgCl [reference electrode (RE), Fig. 1(b)].

The resulting CV curve obtained with a 50 mV/s scan rate and shown in Fig. 1(c) unveils two cathodic current peaks and two anodic current peaks during the reduction (cathodic/negative) and oxidation (anodic/positive) scans, respectively, whereas one of those two peaks in each cycle is narrower than the other. Concerning the standard reduction potentials, E_0, the salient feature of our CV study is the decrease in the obtained reduction potentials,

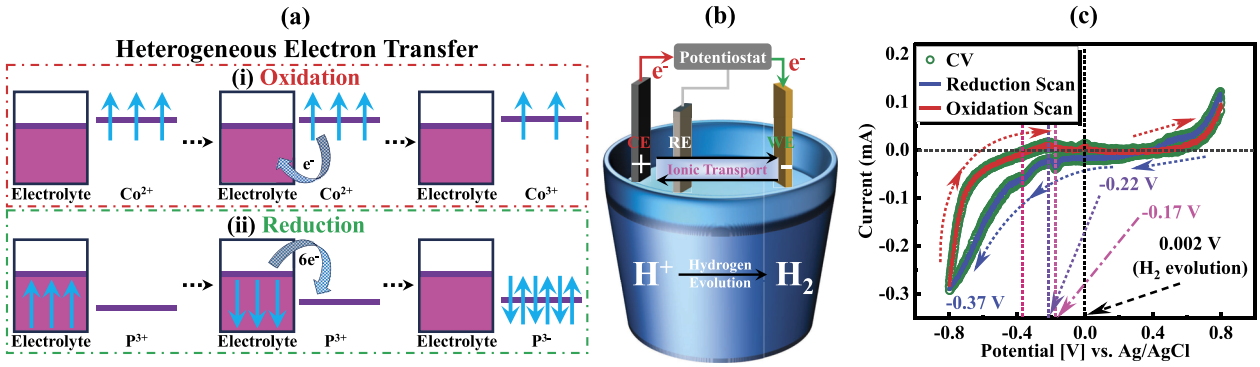


FIG. 1. (a) Heterogeneous electron transfer: (i) oxidation of *Co* and (ii) reduction of *P*. (b) The schematic of the electrochemically controlled NHS formation by hydrogen evolution. (c) A three electrode cyclic voltammogram curve recorded with a standard Ag/AgCl electrode.

05 December 2024 14:20:21

© Author(s) 2024

which happens because of adding saccharine and naphthalene-1,3,6-trisulfonic acid (NTA) in the solution. During the negative scan, in the cathode,

(i) a sharp cathodic peak is obtained at −0.17 V due to the reduction of Co^{2+} in the bath and
(ii) a broad peak is obtained at −0.37 V, which ranges from −0.31 to −0.42 V.

The former cathodic peak at −0.17 V generates possibly due to a faster reduction of Co^{2+} to Co and H_3PO_4 to H_3PO_3, while the latter one generates due to a slow reduction of H_3PO_4. In this region, the nascent-generated H_3PO_3 and the raw H_3PO_3 present in the solution reduce to H_3PO_2 and nonmetallic P, and then, the H_3PO_2 also reduces to nonmetallic P. It was previously believed that the elemental Co and P together form the Co – P amorphous alloy, which provides the low coercivity of the soft material.[38]

As our magnetic study reveals two different coercivities present in a single magnetic material, it is worth assuming that there should be two different phases. So, there must be a different electrochemical mechanism that favors forming a crystalline phase to serve as the source of high coercivity, simultaneously with the amorphous $Co-P$ alloy providing the low coercivity. Hence, we propose the following electrochemical mechanism in forming the nanoheterostructures from a single starting material.

During the cathodic scan, beyond those peaks, the potential sharply falls from the −0.50 to −0.80 V region due to the reduction in nonmetallic P to phosphine (PH_3) and splitting of water (H_2O) molecule. During the positive scan, in the anode, the peaks correspond to the liberation of O_2 and H_2 and oxidation of H_3PO_3 to H_3PO_4. The small peak at −0.002 V corresponds to the evolution of hydrogen. This hydrogen evolution may cause bubbles and internal stress near the cathode. Although those stress-relieving additives were added to the bath, care was taken in such a way that the precipitates just disappeared from the bath and simultaneously ensured the existence of a little amount of stress. As the literature study shows that internal stress causes the hydrogen evolution, the amount of NTA was adjusted to the bath in such a way that it ensured the hydrogen evolution. During the oxidation process, the anode (Co) dissolves in the solution and oxidizes to Co^{3+} and forms an unstable metallic compound, $Co(PH_3)_3$. The nascent unstable metallic compound $[Co(PH_3)_3]$ then spontaneously forms stable amorphous Co – P alloys.[39,40]

The electron configuration of the elemental Co would be Co – hcp having $[Ar]3d^7 4s^2$, and that of the CoP alloy would be the electron configuration of Co^{3+}, i.e., $[Ar]3d^5 4s^1$. According to Hund's rule, half/full–filled $-d$ orbital is more stable than other filled $-d$ orbital; hence, Co^{3+} having the configuration of $3d^5$ has the stable electronic configuration. These two different phases, i.e., the Co – hcp crystalline phase and the amorphous CoP phases, are separated [shown in Fig. 1(a)] due to the hydrogen evolution developed by the stress. Since Co^{3+} is more stable than Co, the formation of $Co-P$ alloys will be preferred than the Co – hcp structures, and hence, a minor fraction of nanocrystalline Co – hcp structures formed due to a faster reduction process of Co^{2+} to Co, as evidenced by the cathodic peak at −0.17 V, would co-exist within the matrix of amorphous $Co-P$ alloys and help build the nanoheterostructured thin film.

Continuous monitoring of pH reveals that the pH of the solution increases after the deposition, as the concentration of $[H^{2+}]$ decreases due to hydrogen evolution and that of $[OH^-]$ increases because of water splitting, generation of PH_3, and elemental P. The electrochemical equations involved in the formation of the NHS structures within the amorphous matrix influenced by the hydrogen evolution, as elucidated in the previous sections are summarized in the following:

$$\mathrm{Co\ (Anode)} \rightleftharpoons \mathrm{Co^{3+}(CoP)} + 3e^-, \tag{R1}$$

$$\mathrm{H_3PO_4} + 2H^+ + 2e^- \rightleftharpoons \mathrm{H_3PO_3} + \mathrm{H_2O}, \tag{R2}$$

$$\mathrm{H_3PO_3} + 2H^+ + 2e^- \rightleftharpoons \mathrm{H_3PO_2} + \mathrm{H_2O}, \tag{R3}$$

$$\mathrm{HPO_3^{2-}} + 2\mathrm{H_2O} + 3e^- \rightleftharpoons \mathrm{P} + 5\mathrm{OH^-}, \tag{R4}$$

$$\mathrm{H_3PO_2} + H^+ + e^- \rightleftharpoons \mathrm{P} + 2\mathrm{H_2O}, \tag{R5}$$

$$\mathrm{P} + 3\mathrm{H_2\,O} + 3e^- \rightleftharpoons \mathrm{PH_3} + 3\mathrm{OH^-}, \tag{R6}$$

$$\mathrm{Co^{3+}} + 3\mathrm{PH_3} \rightarrow \mathrm{Co(PH_3)_3} \rightarrow \mathrm{Co-P}, \tag{R7}$$

$$\mathrm{Co^{2+}} + 2e^- \rightleftharpoons \mathrm{Co}, \tag{R8}$$

$$2H^+ + 2e^- \rightleftharpoons \mathrm{H_2}, \tag{R9}$$

$$2\mathrm{H_2\,O} \rightleftharpoons \mathrm{O_2} + 4H^+ + 4e^-, \tag{R10}$$

$$2\mathrm{H_2\,O} + 2e^- \rightleftharpoons \mathrm{H_2} + 2\mathrm{OH^-}. \tag{R11}$$

B. Structural and stoichiometry analysis

Exploring the quantitative and qualitative analyses of phosphorus (P) in the electrodeposited thin film is of paramount importance due to its significant impact on the crystallinity of CoP thin films.[18,41] The elemental analysis across various regions of the film confirms a consistent stoichiometry. The atomic percentages of cobalt (Co) and phosphorus (P) range from ~86 to 90 and 10 to 14, respectively (see Table II). An EDX spectrum [Fig. 2(a)] validates the presence of Co and P, with the yellow line indicating the EDX line scan path on the film surface. The EDX line scan [Fig. 2(b)] further illustrates the homogeneity in composition, depicting Co and P distribution without any other impurity source. The red and green curves represent the line scan for Co and P, respectively. Any non-identifiable topographic feature of the SEM figure [top image of Fig. 2(b)] unveils the smooth, shiny, and fine-grained surface of the material.

The thicknesses of the electrodeposited films ranging from 0.31 to 14 μm are presented in Table II. The nanoheterostructures, developed via an electrodeposition technique favored by hydrogen evo-

05 December 2024 14:20:21

© Author(s) 2024

TABLE II. Experimentally obtained values of different structural, stoichiometric, and magnetic parameters for various electrodeposited *CoP* thin films.

Current density	Thickness	R_q	$\frac{R_q}{d} \times 100$		$H_C\ (kA/m)$		$B_S\ (T)$		$B_R\ (T)$		$S(M_R/M_S)$	
(mA/cm^2)	(μm)	(nm)	In %	Stoichiometric ratio	Dir-X	Dir-Y	Dir-X	Dir-Y	Dir-X	Dir-Y	Dir-X	Dir-Y
5.48	0.31	3.00	0.967	$Co_{86.80}P_{13.20}$	2.697	2.718	0.472	0.367	0.223	0.193	0.4724	0.5367
10.97	0.68	2.24	0.329	$Co_{87.10}P_{12.90}$	13.41	15.73	0.596	0.814	0.5134	0.701	0.8603	0.8601
16.46	5.06	10.03	0.198	$Co_{88.20}P_{11.80}$	15.31	15.74	1.801	1.587	1.487	1.343	0.8260	0.8464
21.95	11.38	11.54	0.101	$Co_{86.30}P_{13.70}$	12.88	12.96	0.881	0.677	0.780	0.616	0.8958	0.9094
27.44	12.44	12.24	0.098	$Co_{92.34}P_{7.76}$	13.60	13.60	0.987	0.803	0.888	0.728	0.8998	0.9072
32.92	13.36	12.30	0.092	$Co_{91.99}P_{8.07}$	18.18	18.28	1.000	0.936	0.900	0.840	0.8998	0.8982

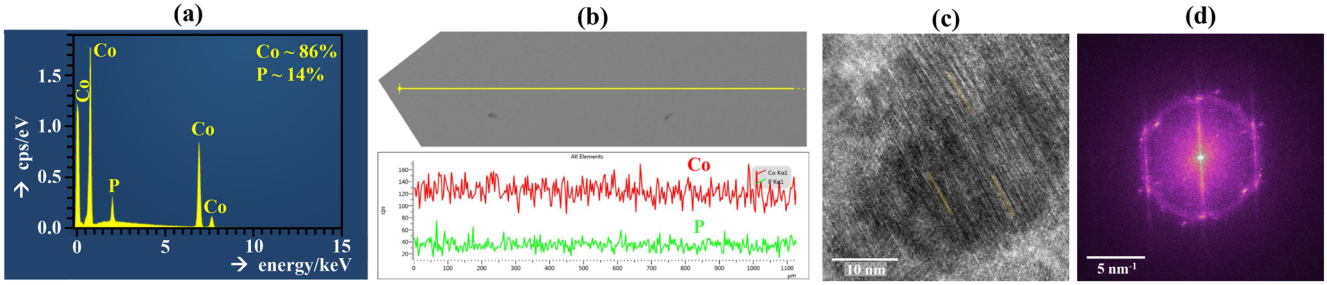


FIG. 2. (a) Typical EDX spectrum showing the presence of *Co* and *P* in the films. (b) Top: EDX line scan path on the surface (yellow line). Bottom: the red curve denotes the line scan for *Co* and the green curve for *P*. (c) A cross-sectional HR-TEM image of the film showing the striations in an nm range formed due to stress caused by *H*−evolution. (d) FFT of the TEM image (c) confirms crystalline phases (*Co* − hcp) present in the amorphous *CoP* matrix.

lution, as explained earlier, have been experimentally observed by the cross-sectional HR-TEM [see Fig. 2(c)]. Here, the 2–5 nm white lines in the HR-TEM image correspond to the *Co* − hcp phases, and the rest of the black regions correspond to the amorphous *CoP* (a few of the white lines are marked with orange lines) from the nanoheterostructured system, where the crystalline *Co* − hcp phases are embedded within the amorphous *CoP* matrix.[18] The crystallinity of the *Co* − hcp phases is further confirmed by performing the fast Fourier transformation (FFT) of the TEM image, as shown in Fig. 2(d).

Figure 3(a) shows the XRD pattern of the prepared amorphous *CoP* thin films. No additional peaks are detected beyond the three dominating substrate peaks: the peak near $2\theta = 69.22°$ corresponds to the Si-wafer, while the other two peaks near $2\theta = 38°$ and $83°$ originate from the top conducting seed layer of gold (Au), confirming the overall amorphous nature of the samples. However, the magnified XRD profiles shown in Figs. 3(b) and 3(c) reveal minor peaks at $2\theta = 44.3°$ and $77.5°$, indicating the presence of nanocrystalline *Co* − hcp(002) and *Co* − hcp(110) phases, respectively. Using the Scherrer equation, the mean grain size of the crystalline phase in the nano-heterostructured film, shown in Fig. 3(d), is calculated to be approximately (3.20 ± 0.57) nm, consistent with the *Co* − hcp stripe thickness obtained from the HR-TEM.

We utilized atomic force microscopy (AFM) to determine the root mean square (RMS) roughness (R_q) of the topographic features, providing quantitative insights from the AFM images. The R_q values are presented in the third column of Table II. Analysis of the results shows that the R_q value increases steadily with the current density during electrodeposition. When the deposition time is 120 minutes with a current density of ~33 mA/cm^2, the R_q value is about four times higher compared to around 5.5 mA/cm^2. However, it decreases by one order of magnitude in terms of the percentage of the overall thickness of the deposited film. This decrease indicates the effectiveness of the bath chemistry, including the proportion of stress-relieving additives, in the plating process. These minor changes are not visible in the SEM images. The significant variation in R_q, ranging from 2.24 nm (minimum) to 12.30 nm (maximum), accompanied by a corresponding decrease in R_q/d from 0.967 (maximum) to 0.092 (minimum), suggests that roughness may contribute to the distribution of nucleation fields.

The spin orientations of the low-current density sample (0.31 μm thick) and comparatively a higher current density sample are shown in Figs. 4(a) and 4(b), respectively. Both the figures reveal almost parallel periodic stripes within a certain region. The white and black stripe pairs in the figure reflect the regions with opposite magnetic orientation, i.e., upward and downward directions. Although the spin stripes shown in Fig. 4(a) are almost straight and regular, a careful observation confirms that they are slightly bent locally. Generally, stripe domains manifests the competition between in-plane and out-of-plane (OOP) anisotropy present in the sample.[19] Coexistence of IP anisotropy simultaneously with the OOP anisotropy in an *in situ* amorphous-nanoheterostructured thin film is elucidated elsewhere.[18]

05 December 2024 14:20:21

© Author(s) 2024

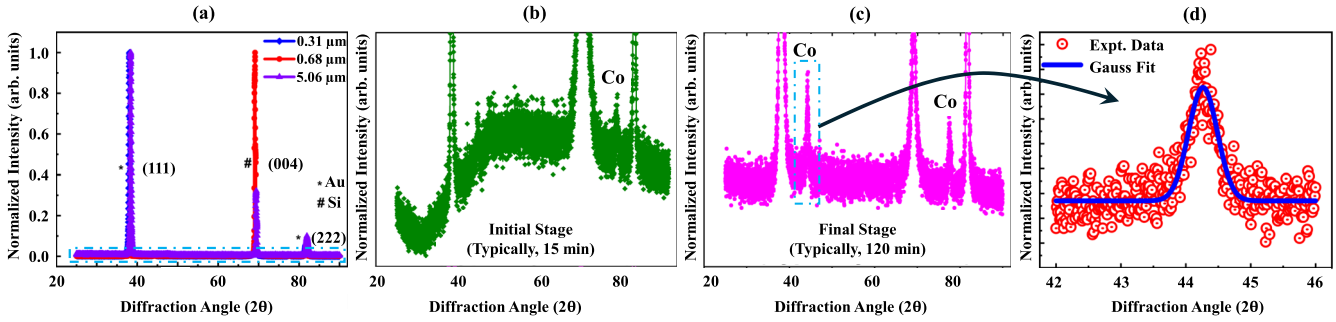


FIG. 3. Structural characterization. (a) XRD spectra of the 0.31, 0.68, and 5.06 μm thick films having three dominant substrate peaks confirming the overall amorphousness of the samples. The magnified XRD spectra of the highlighted region in panel (a) are shown in panel (b) for 0.31 μm film and in panel (c) for 0.68 μm film, respectively. (d) Gaussian fit to the 44° *Co* – hcp peak as marked in panel (c).

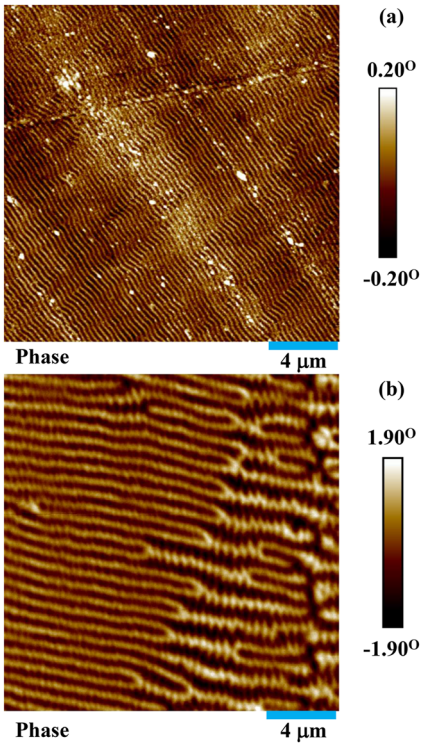


FIG. 4. (a) Typical stripe domain structure in the low-current (~5.5 mA/cm^2) sample. (b) Modified domains featuring corrugated stripes with domain branching in a comparatively higher current ~137 mA/cm^2 sample. Both the scale bars are 4 μm.

In a magnetic thin film with an OOP anisotropy, stray field or magnetostatic energy generated by the interaction between the dipoles favors IP anisotropy. So, in this "*in situ*" NHS system, the competition between IP anisotropy and OOP anisotropy acts as the driving force for stripe domains. As a result, periodic stripes formed where the magnetization rotates in the plane perpendicular to the thin film. This could be the characteristic signature of transverse ES, which we have confirmed later by first-order reversal curve (FORC) measurements and micromagnetic simulations. However, it is worth mentioning here that the reverse might not be always true, i.e., the systems that exhibit stripe domains may not necessarily have a transverse ES state.

Let us define a dimensionless material parameter, $Q = K/K_d$, where K is an appropriate anisotropy (uniaxial or crystalline or shape) constant and K_d is the stray field energy constant. Usually, in a sample with stress-induced OOP anisotropy, the domain bifurcation is favored with a comparatively lower Q value ($Q < 1$, i.e., $K_u < K_d$).[19] From Maxwell's equations, we have seen that the lateral flux is zero, which results into generating the stray field energy. So, the magnetization flux which is entering the area at the base must be dissipated in the interior if practically no flux leaves the finely divided surface. In addition, the nucleation/branching of the domains is perhaps due to the tendency for the spin stripes to remain equidistant and stay in the minimized energy state.[19]

Although the surface was uniform, due to the internal size of the striations (cross sectionally) in the amorphous and nano-heterostructure matrix, the two different phases not only just interact with each other but also they both interact with the out-of-plane anisotropy. The Q parameter of cobalt is too small for this effect, but surface anisotropy adds to the OOP anisotropy for very thin films, so that the effective Q becomes larger than unity[19] and the typical stripe domain gets modulated, leading to the creation of novel corrugated stripe domains.

C. Static magnetic study

Figure 5 shows the experimentally obtained normalized hysteresis loops along the direction X ($dir.X$) and direction Y ($dir.Y$) of those as-prepared materials, where $dir.X$ and $dir.Y$ represent that the measurements were performed on the longitudinal and transverse directions, respectively. Hence, the X and Y directions are two mutually perpendicular directions on the sample plane, i.e., $dir.Y = dir.X + 90^\circ$. The interesting fact for all the normalized hysteresis loops is that both dir. X and dir. Y are practically equivalent, i.e., all the samples are assumed to be magnetically isotropic in the XY plane – a good agreement with the presence of a perpendicular anisotropy.[42] Figure 5(a) shows that the coercivity of 0.31 μm thickness is ~34 Oe $(2.697kA/m)$. Three distinct regions are shown in Fig. 5(a), i.e.,

05 December 2024 14:20:21

© Author(s) 2024

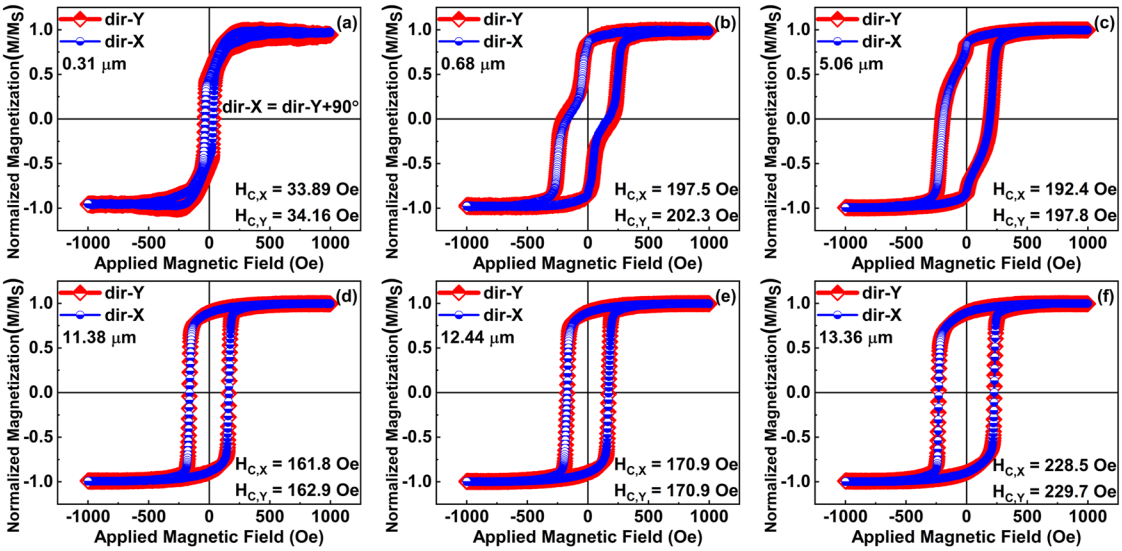


FIG. 5. (a) Non-exchange-spring (ES) of the 0.31 μm sample. (b) ES signature with the 0.68 μm sample. (c) A small kink near ~10 *Oe* observed when the thickness becomes 5.4 μm, showing the OOP anisotropy starts dominating over the IP anisotropy. The ES state becomes a flat EC state, while the thickness is ~11 μm in panel (d) due to the entire domination of the OOP anisotropy over the IP anisotropy. In panels (e) and (f), the flat loops continue with the thicknesses 11.23 and 12.34 μm obtained, respectively. Here, for all the figures, $dir.Y = dir.X + 90^{\circ}$.

(i) at the applied field below ~35 *Oe* ($2.785 kA/m$), the loop shows hysteresis;
(ii) a region at the applied field between 35 Oe and ~500 *Oe* (~ 40 kA/m), where magnetization changes almost linear with the applied field; and finally
(iii) beyond ~500 *Oe*, an unchanged constant magnetization with the applied magnetic field, i.e., the magnetization has been saturated.

Generally, this kind of three-slope hysteresis loop, particularly the region (ii), is the signature of thin films having a weak perpendicular anisotropy[43] that shows magnetic stripe domains, which has already been shown in Figs. 4(a) and 4(b), respectively. However in this case, the in-plane (IP) anisotropy strongly dominates over the weak perpendicular anisotropy. When the sample thickness becomes 0.68 μm, the coercivity increased almost six times to reach ~200 Oe (15.951 kA/m) shown in Fig. 5(b). The observed increments in the thickness and coercivity are qualitatively consistent since nano-heterostructures are formed in this case. Consequently, we obtained the staircase-like hysteresis loop, a signature of the ES structure with two distinguishable coercivities in a single amorphous/nanoheterostructured material shown in Fig. 5(b). Here, the two different phases (namely, *Co* – hcp and amorphous *CoP*) are non-rigidly coupled to each other through the magnetic exchange interaction and act as separate units in the same material. Neither IP nor OOP anisotropy dominates each other. Hence, with the application of an external magnetic field, both the phases reverse at the different magnetic fields. The amorphous CoP phases correspond to the lower coercivity, while the *Co* – hcp phase corresponds to the relatively higher coercivity. While the thickness becomes 5.4 μm, the OOP anisotropy starts dominating over the IP anisotropy. Consequently, a small kink near 10 Oe exists along with the relatively higher coercivity of ~180 *Oe*. The ES structure starts converting to the EC structure, giving rise to a flat hysteresis loop, while the thickness is ~11 μm shown in Fig. 4(d), as in this case, the OOP anisotropy entirely dominates over the IP anisotropy and both the phases act as a single unit. As a result, they reverse at the same field. In Figs. 5(e) and 5(f), the flat nature of the hysteresis loops remains unaltered with the thicknesses of ~12 μm and ~13 μm, respectively. As a result, a high "S" value (M_R/M_S) is shown for Figs. 5(b)–5(f) as presented in Table II.

D. First-order reversal curve (FORC) measurement

So far, the static magnetic study illustrated the complex relationship between magnetization and the applied magnetic field, resulting into different hysteresis loops. However, they are not capable of revealing the presence of magnetic exchange interaction between the phases in the system. For a deeper understanding of magnetic phase interactions at the nanoscale, we extended our analysis to include minor hysteresis loop analysis, specifically through first-order reversal curve (FORC) measurements presented on the (H_C, H_U) plane.

Figures 6(a) and 6(b) show the FORC distributions of 0.31 and 0.68 μm films, respectively. Figure 6(a) shows only one peak at H_C =~ 35 Oe centered at H_U = 0 Oe, which signifies that there is no extra peak except the coercivity in the sample. On the contrary, Fig. 6(b) shows three distinct peaks, two on H_C = 10 Oe ("P1") and H_C =~ 280 Oe ("P2") centered at the H_U =~ −30 Oe axis, while the third one is centered at H_U = −135 Oe on H_C = 160 Oe ("P3"). The third peak, "P3," arises in the 0.68 μm film due to the interaction between the two other peaks present in the system, while the peak

05 December 2024 14:20:21

© Author(s) 2024

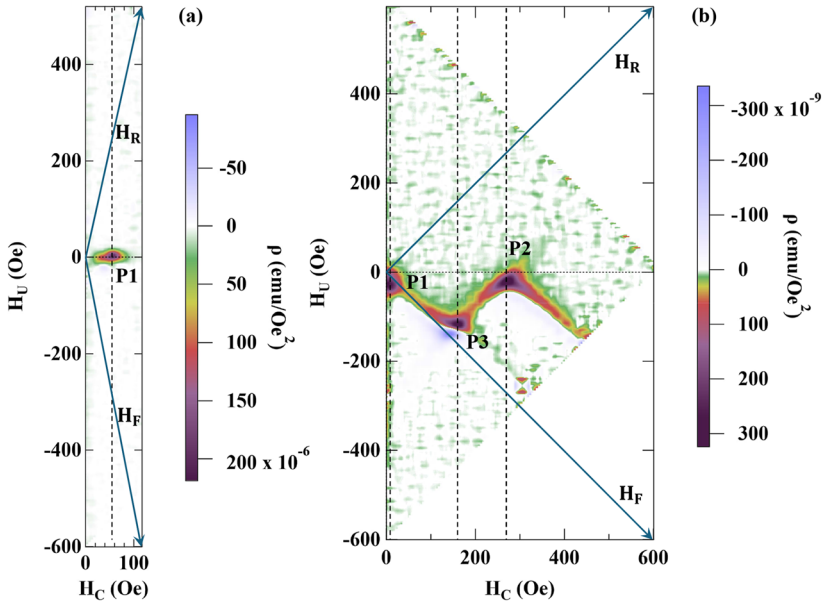


FIG. 6. IP FORC measurement of (a) 0.31 μm and (b) 0.68 μm films in the (H_C, H_U) plane.

"P3" is absent in the 0.31 μm film. Therefore, the 0.31 μm film is the non-exchange-spring (nES) sample, while the 0.68 μm film becomes the (ES) sample. So, in the thicker samples, which exhibited such a staircase-like hysteresis loop, we justifiably assumed that FORC distribution of the same would reveal a similar pattern on the (H_C, H_U) plane.

Although the FORC distribution revealed the magnetic exchange interaction between different phases, it fails to reveal the competition between IP (in-plane) anisotropy and OOP (out-of-plane) anisotropy. Since we observe the signature of weak perpendicular anisotropy with strong IP anisotropy in the 0.31 μm non-ES film, we assume that the OOP anisotropy of the 0.68 μm ES film at some OOP angle might overcome the IP anisotropy and may exhibit transverse ES[13,25] nature. Therefore, we further studied the minor loop measurement of the hysteresis loop, i.e., FORC measurements of the 0.68 μm sample as a function of OOP angle exploring how such magnetic exchange interaction influences pivoting toward the transverse exchange-spring due to the influence of OOP anisotropy.

The raw FORC data, showing individual minor loops of the full hysteresis loop at angles (15°, 30°, 45°, 60°, and 90°) are shown in Fig. 7. The inset shows a schematic of the sample and the applied magnetic field orientation, highlighting the variation of the OOP angle along the z direction due to the rotation of the sample when the magnetic field is oriented perpendicularly. Although we observe initially (in Fig. 5) that the ES film is magnetically isotropic on in-plane, the variation of the moments (first decrease to a certain point and then again start increasing, as highlighted with the curved arrow) in the OOP plane measurement suggests that the sample is magnetically anisotropic along the OOP direction. The 60° data show that it has an elongated loop, which is possibly due to the dominance of strong OOP anisotropy over the IP one.

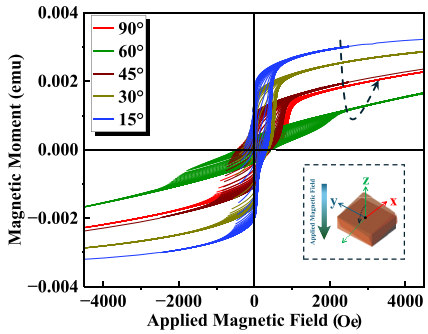


FIG. 7. OOP angle-dependent raw FORC curves of the 0.68 μm film. The inset shows a schematic of the sample and the applied magnetic field orientation, revealing that the OOP angle varies along the z-direction due to the sample rotating, while the magnetic field direction remains fixed perpendicularly.

We have now presented the individual raw data, aiming to confirm the competition between in-plane (IP) and out-of-plane (OOP) anisotropy. In Fig. 8, the raw minor hysteresis loops of various angles are shown, along with magnified versions near the ±0.0005 emu region inset at the bottom right of each figure, alongside their corresponding processed FORC distributions on the (H_C, H_U) plane. In Figs. 8(a) and 8(c), corresponding to 15° and 30° angles, the magnetic moments undergo a smooth transition from negative to positive direction. However, Fig. 8(e) shows that while the magnetic moments originating at $H_F \approx -900$ Oe on the lower side jump directly from the negative side to the positive side, as highlighted in the inset, the magnetic moments originating above $H_F \approx -900$ Oe transition smoothly. It could be attributed that in this angle, the OOP anisotropy component could not dominate

05 December 2024 14:20:21

© Author(s) 2024

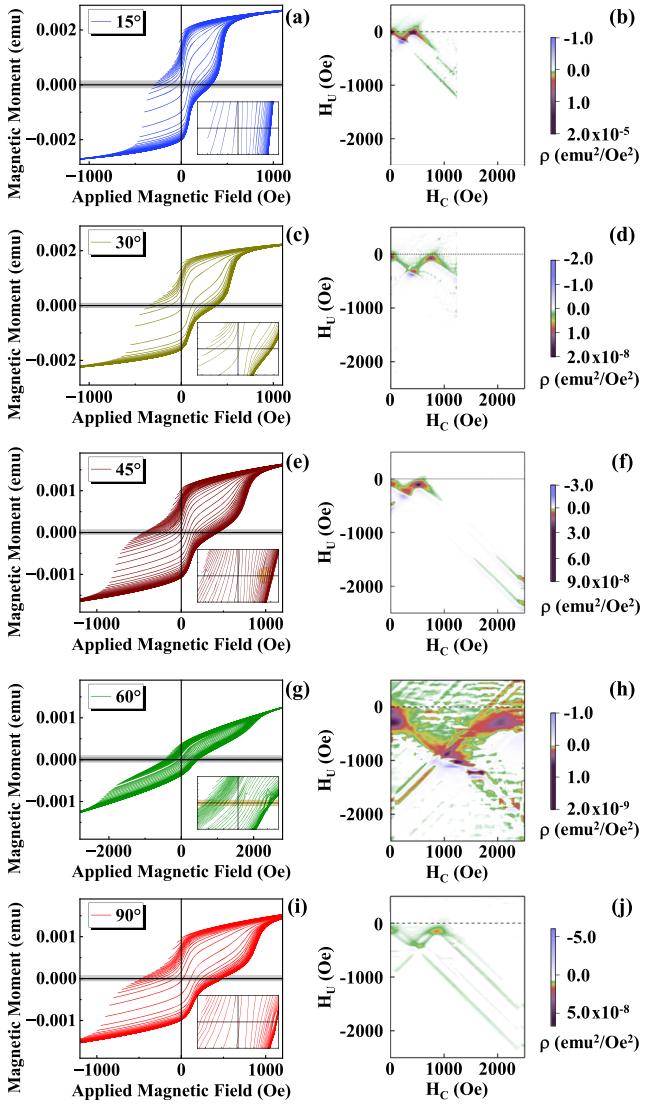


FIG. 8. OOP angle-dependent raw minor loops and its corresponding FORC distribution of the 0.68 μm film indicating transverse ES nature.

over the corresponding IP anisotropy component. The 60° hysteresis loop is almost linear to the applied magnetic field due to the dominance of strong OOP anisotropy. A closer insight at Fig. 8(g) further reveals a distinct jump in the minor hysteresis loop at the 60° angle, where all the magnetic moments shift directly from the negative region to the positive region. Therefore, the distinct FORC behavior observed at 60° could be attributed to changes in OOP magnetic anisotropy as the angle of the applied field varies. At this angle, the anisotropy energy landscape might shift, leading to different magnetic domain configurations or reversal mechanisms. This could result in unique features in the FORC diagram that are not present at other angles. In contrast, at other angles, the transition of the moments occurs smoothly, indicating the establishment of an anisotropy-driven metastable state at 60°.

This results in a significant change in the 60° FORC distribution compared to other FORC diagrams. Interestingly, as the OOP angle increases, both the H_C and H_U values in the corresponding FORC diagrams also increase, peaking at 60° before decreasing. This suggests that the dominance of the OOP component becomes apparent for some moments at 45° and is prominent at 60° due to instability caused by strong competition between in-plane (IP) anisotropy and out-of-plane (OOP) anisotropy. Despite stabilizing the applied magnetic field at each point (utilizing an in-built feature of the QD MPMS3 system) during measurements, minor abrupt shifts in magnetic moments around the transition zone in the minor loop are observed, as shown in Fig. 8(g)-inset. This strong competition may not only cause these abrupt shifts in magnetic moments but also the significant change in the ρ distribution in the corresponding FORC diagram.

This phenomenon is consistent with previous findings, where the competition between IP and OOP anisotropy leads to a sudden jump in the hysteresis loop and the establishment of a metastable state.[26] Consequently, we infer that between angles 60°–90°, another phase contributes to the exchange-spring (transverse), which may be suppressed at other angles by a dominant phase. Thus, in the case of such amorphous and nanocrystalline films, the in-plane exchange-spring may tend to convert to the transverse exchange-spring due to the effect of the emerging metastable state.

E. Micromagnetic simulations

In order to elucidate the experimentally obtained results of the nanoheterostructured thin films, we further performed micromagnetic simulation using MuMax^3.[32] An external image, as shown in Fig. 9(a) (nearest approximation), was utilized in the simulation to make the geometry comparable with the experimentally obtained dispersed NHS. In the simulation, each of the dispersed black lines with an average thickness of 3.50 nm is assumed as crystalline *Co* – hcp with OOP anisotropy along the (0,0,1) direction, while the remaining blank portion represents as amorphous CoP with IP anisotropy along the (1,1,0) direction. It is noted that $-X, Y, Z$ signify the $-x, y, z$ directions of the geometry, respectively.

We considered different values for the typical magnetic material parameters such as saturation magnetization (M_S), exchange stiffness constant (A_{ex}), anisotropy constant (K_{u1}) as 815×10^3 A/m, 10×10^{-12} J/m, and 1.232×10^3 J/m^3 for *CoP* and 1400×10^3 A/m, 30×10^{-12} J/m, and 520×10^3 J/m^3 for *Co* – hcp, respectively. We considered the cell size in each direction lower than the exchange length $\left(l_{ex} = \sqrt{\frac{A_{ex}}{K_d}} = \sqrt{\frac{2A_{ex}}{\mu_0 M_S^2}} = 4.94 \text{ nm and } 4.89 \text{ nm for CoP and Co – hcp, respectively}\right)$[19] of the system ensuring the inclusion of all exchange interactions properly. The simulations have been performed with cell size = $3 \times 3 \times 3$ nm^3 and the simulation grid size = $512 \times 512 \times 128$, which results the final volume of the simulation = $1536 \times 1536 \times 384$ nm^3. We note that here, $-X, Y, Z$ signify the $-x, y, z$ directions of the geometry, respectively.

Figure 9(b) shows that the typical three-slope hysteresis loop, as shown in Fig. 5(a), obtained from the simulation. "*" marked positions shown in Figs. 9(b) and 9(d) are the nucleation state, the signature of the formation of the weak perpendicular anisotropy. The cross-sectional view of the macro-spin configuration of "*" marked position in Fig. 9(b) is shown in Fig. 9(c),

05 December 2024 14:20:21

© Author(s) 2024

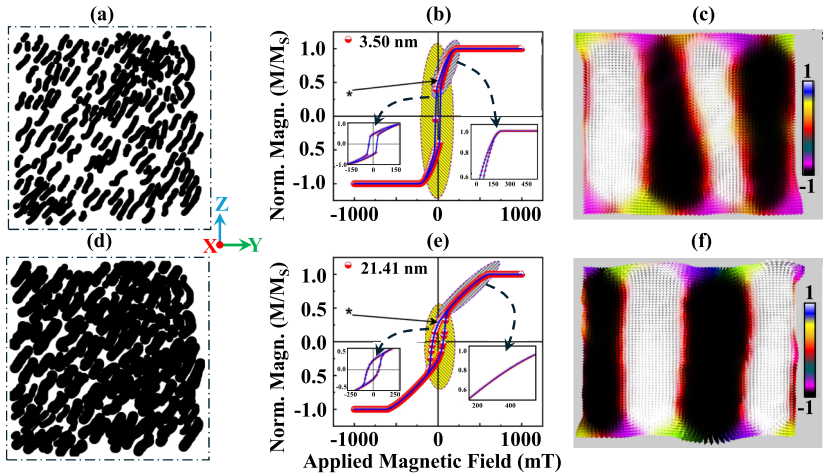


FIG. 9. (a) Average of dispersed 3.50 nm thick NHS utilized as an input image in the simulation at YZ plane. (b) Simulated three-slope hysteresis loop with the complex geometry. (c) Cross-sectional macro-spin behavior of "*" marked position in the hysteresis loop. (c) Thick NHS. (d) ≈ 6 times dense 21.41 nm thick NHS utilized as an input image in the YZ plane. (e) The simulated large hysteresis loop considering the NHS in panel (c). (f) The macro-spin behavior as marked in panel (e).

where the red and green arrows represent moments along $+x$ and $-x$ directions, respectively. The cross-sectional view reveals that the slight distorted stripes are formed with alternate upward (white) and downward (black) moments throughout the cross section, respectively.

To get more insight into the formation of the stripes in the simulation, we have calculated the quality factor defined as $Q = K/K_d$, where K and K_d are the appropriate anisotropy and the stray field coefficient of the system, respectively. Since units of K and K_d are the same, Q is a dimensionless quantity. Theoretically, it has been proven that stripe formation is favored by low or moderate Q values (i.e., $Q \ll 1$ or $Q \simeq 1$) of the system.[19] To validate the effect of the thickness of the NHS in the formation of stripes and its orientation, other sets of simulation have been studied with different thickness of NHSs. By simulation, we have identified that the critical limit of average thickness of NHS lies between 9.78 and 12.66 nm when the stripes change their orientation. In addition, subsequently, enhancement in coercivity has been observed. Here, comparatively more denser 21.41 nm thick NHS beyond the obtained critical limit is considered, as shown in Fig. 9(d), while the rest of conditions during the simulations remains unchanged.

As discussed, the denser NHS results in the hysteresis loop with an enhanced coercivity, as shown in Fig. 9(e), would also help increase the energy product ($BH_{\max}$) of the material. Interestingly, in comparison with the stripe domains shown in Fig. 9(c), a significant change in the stripe domains is visible, as shown in Fig. 9(f), although both the macro-spin behaviors shown in Figs. 9(c) and 9(f) are taken at the same applied field value from the simulation. The upward and downward moments not only change their positions but also the stripes of Fig. 9(f) are more aligned and straight than that of Fig. 9(c). The enhancement of the OOP anisotropy in the latter case associated with the broadening of the NHS widths might be responsible in stabilizing the stripe domains.

To quantify the variation of the stripe obtain from the simulations shown in Figs. 9(c) and 9(f), we calculated the variation of energies, such as exchange energy, anisotropy energy, demagnetization energy, and total energy of those two NHSs as a function of applied magnetic field, as shown in Figs. 10(a)–10(d), respectively. Since the width of the NHS increases in Fig. 9(d) compared to Fig. 9(a), the strength of the exchange interaction between the $(0, 0, 1)$ spins and the $(1, 1, 0)$ spins are much stronger in the NHS of Fig. 9(d) than that of Fig. 9(a). As a result, the exchange energy increases for the 21.41 nm wide NHS compared to that of 3.50 nm wide NHS, as shown in Fig. 10(a). The Q parameter of OOP Co – hcp is small ($Q \approx 0.4$); however, surface anisotropy plays a key role in increasing the OOP anisotropy for 3.50 nm wide NHS, and as a result, the effective Q becomes larger than unity. However, the relative influence of surface anisotropy decreases with the increasing widths of the NHSs, which results into a decrease in the anisotropy energy, as shown in Fig. 10(b). Since the demagnetizing field/magnetostatic energy depends on the shape and volume, the demagnetization energy increases because of the increasing widths of the NHS, as shown in Fig. 10(c), which favors the formation of the stripe domains. However, beyond a critical thickness of the nanoheterostructure (here, greater than 12.66 nm), the contribution of the shape in demagnetization energy shown in Fig. 10(c) becomes apparent with the change in the slope of the decrease and consequently the slope of the variation of the demagnetization energy for denser sample crosses over the slopes of the others. As shown in Fig. 10(d), the total energy for the denser NHS [Fig. 9(d)] is comparatively lower than the thinly dispersed NHS [Fig. 9(a)], which might be responsible in the stabilization of the stripe domains.

The dimensionless parameter, Q, plays an important role in determining the applicability of a material and explaining the formation of domain structures. Usually, the soft magnetic materials have $Q \ll 1$, while the condition $Q \gg 1$ favors a material to be a strong permanent hard magnet. As both the values of Q_{IP} and Q_{OOP} (0.003 and 0.422, respectively) satisfy the theoretical framework, here stripe domains are formed in the simulation, as shown in Figs. 9(c) and 9(e). Since the recording media should have to be

05 December 2024 14:20:21

© Author(s) 2024

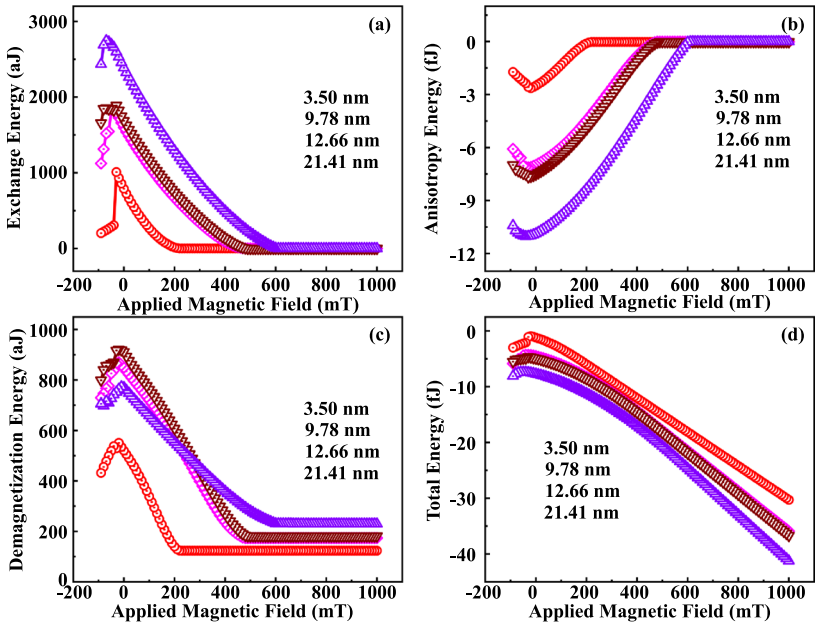


FIG. 10. Variation of simulated (a) exchange energy, (b) anisotropy energy, (c) demagnetization energy, and (d) total energy as a function of applied magnetic field for different widths of the NHS.

05 December 2024 14:20:21

both permanent and easy to switch, materials should consist of neither high nor low anisotropy, i.e., moderate anisotropy value should be desirable. Although magnetic hardness is not directly related to the properties of high and low relative anisotropy, i.e., the high and low coercivity. In conjunction with the magnetic microstructure, other additional structural features such as lattice defects, grain boundaries, sample or particle size, and surface irregularities are also important to determine the coercivity of the material. The intrinsic Q parameter determines the ease with which a desired magnetic hardness (or softness) can be achieved. Now, if a system is built with an intrinsic stripe domain structure, the Q value should satisfy the criteria, i.e., $Q < 1$ or $Q \approx 1$, i.e., with this $Q \approx 1$ condition, the desired criteria of the recording media have already been achieved. Moreover, the system does not require any external agitation such as ac demagnetization or thermal perturbations for modulating the parameters and thereby can serve as a building block for recording media.[19,25] In addition, the ES structures with non-collinear anisotropies, i.e., the transverse ES springs with canted interfacial moments can potentially be tuned to facilitate the absorbed spin current to exert an even greater torque for optically induced magnetization precession in spin transfer torque (STT) devices, thus providing a path for improving the efficiency of such devices to a great extent.[19,25]

We have further performed dynamic simulations[44] by solving the Landau–Lifshitz–Gilbert (LLG) equation [Eqs. (1) and (2)],

$$\frac{\partial \vec{M}}{\partial t} = |\gamma|\vec{M} \times H_{\text{eff}} + \frac{\alpha}{M_S}\left[\vec{M} \times \frac{\partial \vec{M}}{\partial t}\right], \tag{1}$$

$$H_{\text{eff}} = -\frac{1}{\mu_0} \cdot \left[\frac{\partial E}{\partial \vec{M}}\right]. \tag{2}$$

In these equations, $\vec{m}$ represents the unit vector of local magnetization; $\gamma_0 = \mu_0|\gamma|$ is the product of the free space permeability and the magnitude of the gyromagnetic ratio (GHz/T); and $\vec{H}_{\text{eff}}$ is the effective magnetic field arising from demagnetization energy, exchange energy, and magnetic and shape anisotropy. The parameter α is the Gilbert damping factor, μ_0 is the free space permeability, and M_S is the saturation magnetization (A/m).

We have shown the calculated magnetization component (M_X) of a typically mimicked NHS system as a function of an external applied magnetic field shown in Fig. 8(a). It is evident that the initial unstability in magnetization oscillation has been diminished when the applied magnetic field is 1 T. At 1 T, the oscillation decays rapidly (fast damping) within ~0.35 nm and 0.41 ns and after that the oscillation starts precessing. A closure look in 1.5 and 2 T data reveals that after the fast decay/damping mode, the oscillation has a beating period of ≈1.31 ns and ≈1.15 ns. Beyond a particular field (1 T), the observed damped oscillatory behavior upto a simulation time, followed by a beating precessional pattern, in calculated magnetization oscillations, as shown in Fig. 11(a), could be attributed to the coexistence of both the fundamental Kittel mode and the perpendicular standing spin wave (PSSW) mode in the system. The corresponding fast Fourier transform (FFT) spectra shown in Fig. 11(b) yields the corresponding power spectra of that NHS system as a function of applied magnetic field. Therefore, as shown in Fig. 11(b), it could be expected that the system developed with such material and

© Author(s) 2024

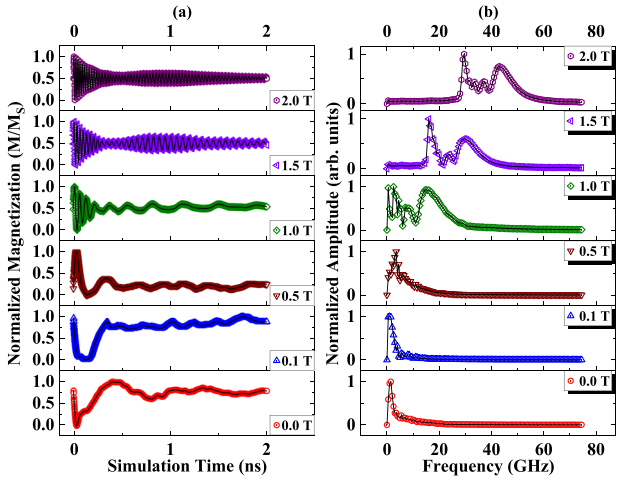


FIG. 11. (a) Typical field dependent calculated magnetization oscillations of the NHS system. (b) Corresponding power-frequency spectra of the system.

its derivatives potentially could be operated at 1.5 GHz without an external field and at ~44 GHz when an external bias magnetic field of 2 T is applied.

IV. CONCLUSION

Utilizing the conventional DC electrodeposition technique, the nano-heterostructured transverse exchange-spring (ES) amorphous/nanocrystalline magnetic thin films have been fabricated *in situ* from a single starting material through the electrochemical control of hydrogen evolution within the system. Our study offers an approach to prepare the transverse exchange-spring and exchange coupled (EC) structure in a cost-effective and scalable manner, opening the door to modify the bulk magnetic properties even in a single ferromagnetic thin film and further the study of exchange-spring mechanism evolving to exchange coupled state via transverse exchange-spring in single amorphous/nanocrystalline film. The quasi-static magnetic properties of nanoheterostructured CoP thin films characterized by magnetic stripe domains at remanence have been investigated both experimentally and by performing micromagnetic simulations. The signature of the stripe domains and its modification (the corrugated stripes) are prominently observed in the MFM and hysteresis loop measurements and supplemented by micromagnetic simulations. The existence of the OOP anisotropy in the system is confirmed by MFM, first-order reversal curve (FORC) measurements and micromagnetic simulations. Micromagnetic study further confirms that the thicknesses of the nano-heterostructures influence the nature of the hysteresis in such an amorphous/nanocrystalline film. The increment in the coercivity and energy product in the ES and EC structures, and the performed micromagnetic simulations demonstrated here, provides a wonderful opportunity to use these materials and their derivatives for next-generation spintronic devices.

ACKNOWLEDGMENTS

A.S. thanks Pawel Gruszecki of Adam Mickiewicz University, Poland, for helpful discussions regarding micromagnetic simulation. The authors acknowledge Science Foundation Ireland (SFI) Frontiers for the Future Programme (FFP) Award Grant (Grant No. SFI-21/FFP-A/10003-MERIT) and NSF-SFI-DFE within the tripartite US-Ireland program (the associated Irish project Grant No. SFI-22/US/3852-nano-antenna) for funding this work.

AUTHOR DECLARATIONS

Conflict of Interest

The authors have no conflicts to disclose.

Author Contributions

S.R. conceived the idea, designed the project to bring the necessary research grant. A.S. prepared the samples and carried out the measurements, performed the micromagnetic simulations. A.S. took a major role in analyzing the data and writing the original draft of the manuscript in conjunction with S.R.

Arindam Samanta: Conceptualization (equal); Data curation (lead); Formal analysis (lead); Investigation (lead); Methodology (lead); Software (lead); Validation (lead); Writing – original draft (lead); Writing – review & editing (equal). **Saibal Roy**: Conceptualization (lead); Data curation (supporting); Formal analysis (supporting); Funding acquisition (lead); Project administration (lead); Resources (lead); Supervision (lead); Writing – original draft (supporting); Writing – review & editing (lead).

DATA AVAILABILITY

The data that support the findings of this study are available from the corresponding author upon reasonable request.

REFERENCES

[1] E. F. Kneller and R. Hawig, "The exchange-spring magnet: A new material principle for permanent magnets," IEEE Trans. Magn. **27**, 3588–3560 (1991).
[2] E. E. Fullerton, J. S. Jiang, M. Grimsditch, C. H. Sowers, and S. D. Bader, "Exchange-spring behavior in epitaxial hard/soft magnetic bilayers," Phys. Rev. B **58**, 12193–12200 (1998).
[3] H. Zeng, J. Li, J. P. Liu, Z. L. Wang, and S. Sun, "Exchange-coupled nanocomposite magnets by nanoparticle self-assembly," Nature **420**, 395–398 (2002).
[4] E. E. Fullerton, J. Jiang, and S. Bader, "Hard/soft magnetic heterostructures: Model exchange-spring magnets," J. Magn. Magn. Mater. **200**, 392–404 (1999).
[5] H. D. Chopra, M. R. Sullivan, A. Ludwig, and E. Quandt, "Magnetoelastic and magnetostatic interactions in exchange-spring multilayers," Phys. Rev. B **72**, 054415 (2005).
[6] J. E. Davies, O. Hellwig, E. E. Fullerton, J. S. Jiang, S. D. Bader, G. T. Zimányi, and K. Liu, "Anisotropy dependence of irreversible switching in Fe/SmCo and FeNi/FePt exchange spring magnet films," Appl. Phys. Lett. **86**, 262503 (2005).
[7] D. Suess, "Multilayer exchange spring media for magnetic recording," Appl. Phys. Lett. **89**, 113105 (2006).
[8] J. McCord, L. Schultz, and J. Fassbender, "Hybrid soft-magnetic lateral exchange spring films prepared by ion irradiation," Adv. Mater. **20**, 2090–2093 (2008).

05 December 2024 14:20:21

© Author(s) 2024

[9]Y. Liu, Y. Q. Wu, M. J. Kramer, Y. Choi, J. S. Jiang, Z. L. Wang, and J. P. Liu, "Microstructure analysis of a SmCo/Fe exchange spring bilayer," Appl. Phys. Lett. **93**, 192502 (2008).
[10]D. Roy and P. S. A. Kumar, "Enhancement of $(BH)_{max}$ in a hard-soft-ferrite nanocomposite using exchange spring mechanism," J. Appl. Phys. **106**, 073902 (2009).
[11]P. Krone, D. Makarov, T. Schrefl, and M. Albrecht, "Exchange coupled composite bit patterned media," Appl. Phys. Lett. **97**, 082501 (2010).
[12]S. Sawatzki, R. Heller, C. Mickel, M. Seifert, L. Schultz, and V. Neu, "Largely enhanced energy density in epitaxial $SmCo_5$/Fe/$SmCo_5$ exchange spring trilayers," J. Appl. Phys. **109**, 123922 (2011).
[13]G. B. G. Stenning, G. J. Bowden, S. A. Gregory, P. A. J. de Groot, G. van der Laan, L. R. Shelford, P. Bencok, P. Steadman, A. N. Dobrynin, and T. Hesjedal, "Transverse magnetic exchange springs in a $DyFe_2$/YFe_2 superlattice," Phys. Rev. B **86**, 174420 (2012).
[14]A. Haldar, C. Banerjee, P. Laha, and A. Barman, "Brillouin light scattering study of spin waves in NiFe/Co exchange spring bilayer films," J. Appl. Phys. **115**, 133901 (2014).
[15]W. Si, G. P. Zhao, N. Ran, Y. Peng, F. J. Morvan, and X. L. Wan, "Deterioration of the coercivity due to the diffusion induced interface layer in hard/soft multilayers," Sci. Rep. **5**, 16212 (2015).
[16]D. J. Carnevale, M. Shatruk, and G. F. Strouse, "Ligand passivated core–shell FePt@Co nanomagnets exhibiting enhanced energy product," Chem. Mater. **28**, 5480–5487 (2016).
[17]Q. Zhao, X. He, F. Morvan, X. Zhang, G. Zhao, Z. Li, L. Li, and Y. Liu, "Interface layer thickness dependence of magnetic properties of SmCo/Fe exchange-spring multilayers: An analytical micromagnetic approach," J. Magn. Magn. Mater. **495**, 165858 (2020).
[18]A. Samanta, G. Gubbiotti, and S. Roy, "Spin waves in exchange spring nanoheterostructured amorphous/nanocrystalline films," Phys. Rev. B **107**, 214449 (2023).
[19]A. Hubert and R. Schäfer, *Magnetic Domains: The Analysis of Magnetic Microstructures* (Springer Science+Business Media, 2008), Chaps. 3 and 5.
[20]O. Hellwig, A. Berger, J. B. Kortright, and E. E. Fullerton, "Domain structure and magnetization reversal of antiferromagnetically coupled perpendicular anisotropy films," J. Magn. Magn. Mater. **319**, 13–55 (2007).
[21]S. Dobák, J. Füzer, I. Petryshynets, P. Kollár, and F. Kováč, "Enhanced soft-to-hard magnetic switching ratio in grain-oriented Fe–Si cores induced by helical anisotropy," Appl. Phys. Lett. **123**, 242406 (2023).
[22]G. B. G. Stenning, A. R. Buckingham, G. J. Bowden, R. C. C. Ward, G. van der Laan, L. R. Shelford, F. Maccherozzi, S. S. Dhesi, and P. A. J. de Groot, "Exchange-spring-driven spin flop in an $ErFe_2$/YFe_2 multilayer studied by x-ray magnetic circular dichroism," Phys. Rev. B **84**, 104428 (2011).
[23]T. N. A. Nguyen, Y. Fang, V. Fallahi, N. Benatmane, S. M. Mohseni, R. K. Dumas, and J. Åkerman, "[Co/Pd]–NiFe exchange springs with tunable magnetization tilt angle," Appl. Phys. Lett. **98**, 172502 (2011).
[24]P. Saravanan, J.-H. Hsu, C. L. Tsai, C. Y. Tsai, Y. H. Lin, C. Y. Kuo, J.-C. Wu, and C.-M. Lee, "Interplay between out-of-plane anisotropic L11-type CoPt and in-plane anisotropic NiFe layers in CoPt/NiFe exchange springs," J. Appl. Phys. **115**, 243905 (2014).
[25]M. Dabrowski, A. Frisk, D. M. Burn, D. G. Newman, C. Klewe, A. T. N'Diaye, P. Shafer, E. Arenholz, G. J. Bowden, T. Hesjedal, G. van der Laan, G. Hrkac, and R. J. Hicken, "Optically and microwave-induced magnetization precession in [Co/Pt]/NiFe exchange springs," ACS Appl. Mater. Interfaces **12**, 52116–52124 (2020).
[26]T. Maity, S. Li, L. Keeney, and S. Roy, "Ordered magnetic dipoles: Controlling anisotropy in nanomodulated continuous ferromagnetic films," Phys. Rev. B **86**, 024438 (2012).
[27]G. B. G. Stenning, G. J. Bowden, S. A. Gregory, J.-M. L. Beaujour, P. A. J. de Groot, G. van der Laan, L. R. Shelford, P. Bencok, P. Steadman, A. N. Dobrynin, and T. Hesjedal, "Magnetic reversal in a YFe_2 dominated $DyFe_2$/YFe_2 multilayer film," Appl. Phys. Lett. **101**, 072412 (2012).
[28]J. P. Liu, C. P. Luo, Y. Liu, and D. J. Sellmyer, "High energy products in rapidly annealed nanoscale Fe/Pt multilayers," Appl. Phys. Lett. **72**, 483–485 (1998).
[29]S. Roy, A. Connell, M. Ludwig, N. Wang, T. O'Donnell, M. Brunet, P. McCloskey, C. ÓMathúna, A. Barman, and R. Hicken, "Pulse reverse plating for integrated magnetics on Si," J. Magn. Magn. Mater. **290–291**, 1524–1527 (2005).
[30]P. McCloskey, B. Jamieson, T. O'Donnell, D. Gardner, M. A. Morris, and S. Roy, "Electrodeposited amorphous Co–P based alloy with improved thermal stability," J. Magn. Magn. Mater. **322**, 1536–1539 (2010).
[31]D. Mallick, K. Paul, T. Maity, and S. Roy, "Magnetic performances and switching behavior of Co-rich CoPtP micro-magnets for applications in magnetic MEMS," J. Appl. Phys. **125**, 023902 (2019).
[32]A. Vansteenkiste, J. Leliaert, M. Dvornik, M. Helsen, F. Garcia-Sanchez, and B. Van Waeyenberge, "The design and verification of MuMax3," AIP Adv. **4**, 107133 (2014).
[33]J. Riveiro and M. Sanchez-Trujillo, "Magnetic anisotropy of electrodeposited Co–P amorphous alloys," IEEE Trans. Magn. **16**, 1426–1428 (1980).
[34]R. J. Harrison and J. M. Feinberg, "FORCinel: An improved algorithm for calculating first-order reversal curve distributions using locally weighted regression smoothing," Geochem., Geophys., Geosyst. **9**, Q05016, https://doi.org/10.1029/2008GC001987 (2008).
[35]D. A. Gilbert, G. T. Zimanyi, R. K. Dumas, M. Winklhofer, A. Gomez, N. Eibagi, J. L. Vicent, and K. Liu, "Quantitative decoding of interactions in tunable nanomagnet arrays using first order reversal curves," Sci. Rep. **4**, 4204 (2014).
[36]D. A. Gilbert, P. D. Murray, J. De Rojas, R. K. Dumas, J. E. Davies, and K. Liu, "Reconstructing phase-resolved hysteresis loops from first-order reversal curves," Sci. Rep. **11**, 4018 (2021).
[37]R. Egli, "VARIFORC: An optimized protocol for calculating non-regular first-order reversal curve (FORC) diagrams," Glob. Planet. Change **110**, 302–320 (2013).
[38]M. T. Tung, L. T. T. Hang, L. A. Tuan, N. H. Nghi, and M.-H. Phan, "Influence of electrodeposition parameters on the magnetic and magneto-impedance properties of CoP/Cu wires," Physica B **442**, 16–20 (2014).
[39]Y. Zeng and S. Zhou, "In situ surface Raman study of the phosphorus incorporation mechanism during electrodeposition of Ni–P alloys," J. Electroanal. Chem. **469**, 79–83 (1999).
[40]K. Sridharan and K. Sheppard, "Electrochemical characterization of Fe-Ni-P alloy electrodeposition," J. Appl. Electrochem. **27**, 1198–1206 (1997).
[41]S. Dutta, A. Samanta, S. N. Panda, S. Roy, and A. Barman, "Ultrafast demagnetization and Gilbert damping in electrodeposited CoP film," J. Mater. Sci. **58**, 14817–14830 (2023).
[42]G. Ausanio, V. Iannotti, L. Lanotte, M. Carbucicchio, and M. Rateo, "Weak stripe domains in Co/Fe multilayers," J. Magn. Magn. Mater. **226–230**, 1740–1742 (2001).
[43]Y. Sun, W. Li, P. Dhagat, and C. R. Sullivan, "Perpendicular anisotropy in granular Co–Zr–O films," J. Appl. Phys. **97**, 10N301 (2005).
[44]A. Samanta and S. Roy, "Generation of microwaves with tuneable frequencies in ultracompact 'magnon microwave antenna' via phonon-magnon-photon coupling," IEEE Trans. Electron Devices **70**, 335–342 (2023).

05 December 2024 14:20:21

© Author(s) 2024